Acta Geotechnica (2025) 20:5203–5219
https://doi.org/10.1007/s11440-025-02660-5

RESEARCH PAPER

Characterizing internal flow mechanisms in reverse extrusion tests using X-ray CT and marker tracking

Shuoshuo Xu[1,3] · Jinxing Lai[1] · Brendan C. O'Kelly[2] · Budi Zhao[3]

Received: 11 December 2024 / Accepted: 9 May 2025 / Published online: 12 June 2025

Abstract
The reverse extrusion (RE) test has been used to evaluate the undrained shear strength of fine-grained soils, but its interpretation is complicated by uncertainties in failure mechanisms. This study adopts X-ray computed tomography (CT) combined with a marker-based tracking method to characterize internal flow patterns during RE testing of kaolinite samples prepared at different water contents. Fine sand particles embedded within the samples served as tracking markers, enabling detailed characterization of internal deformation through sequential X-ray CT scans and advanced image processing techniques. An artificial neural network (ANN) model was developed to enhance marker linkage between scans, using optimized searching zones based on the axisymmetric displacement fields. The analysis revealed two distinct deformation regions for the tested samples, largely independent of soil water content. Near the loading ram, significant radial inward soil displacements created a dome-shaped shear failure surface, driving soil extrusion to occur via the central orifice. In contrast, the region nearest the closed end of the sample chamber exhibited minimal soil displacement, being somewhat influenced by sidewall friction, entrained air bubbles, and stress transfer from the extrusion zone. The observed deformation patterns, characterized by arched shear surfaces and stress rotation zones, differ significantly from previously assumed RE models. These findings highlight the need to refine RE test interpretations, as applied to fine-grained soils, in order to account for complex internal flow mechanisms, chamber sidewall friction effects, and the presence of entrained air bubbles, which would result in improved reliability of RE undrained shear strength measurements.

Keywords Clays · Non-destructive testing · Particle tracking · Reverse extrusion test · Undrained shear strength · X-ray CT

Abbreviations

a	Major particle dimension
ANN	Artificial neural network
AR	Aspect ratio parameter
b	Intermediate particle dimension
c	Minor particle dimension
CT	Computed tomography
c_u	Undrained shear strength
c^*_u	Shear strength mobilized at the sidewall interface
d_a	Axial displacement
d_c	Circumferential displacement
d_r	Radial displacement
L	Half of the side length (of cubic search zone)
L_p	Half of the optimized side length (of cubic search zone)
Lp_z	Optimized base length (of isosceles triangular prism search zone)
Lp_{xy}	Optimized perpendicular height (of isosceles triangular prism search zone)
LVDT	Linear-variable differential transformer
R	Extrusion ratio
RE	Reverse extrusion
SA	Surface area parameter
SP	Sphericity parameter
u_x	Displacement vector along x-axis

✉ Budi Zhao
budi.zhao@ucd.ie

Shuoshuo Xu
shuoshuo.xu@ucd.ie

Jinxing Lai
laijinxing@chd.edu.cn

[1] School of Highway, Chang'an University, Xian, China

[2] Department of Civil, Structural and Environmental Engineering, Trinity College Dublin, Dublin D02 PN40, Ireland

[3] School of Civil Engineering, University College Dublin, Dublin, Ireland

v_y	Displacement vector along y-axis
w_z	Displacement vector along z-axis
w	Water content
V	Volume parameter

1 Introduction

The failure mechanisms in fine-grained soil deposits determine the capacity and safety of geotechnical infrastructures, including shallow and deep foundations, embankment dams, and slopes [5, 18, 19, 24]. For example, Terzaghi's bearing capacity theory predicts the loading capacity of shallow foundations by considering the failure mechanisms within a plastic soil deposit under a strip load [7]. Meanwhile, various experimental tests measuring the shear strength of soils, e.g., direct shear test, triaxial test, fall-cone test, rely on the assumed failure mechanisms in clay samples [22, 26, 34]. Additionally, the reverse extrusion (RE) test offers a practical means to quantify the undrained shear strength (c_u) of fine-grained soils by measuring the extrusion pressure (p_e) [13–15, 35]. This method involves compressing a soil sample in a cylindrical container and extruding it through a small orifice. Previous RE results showed that the p_e value correlates well with c_u at various water contents for a specific soil type [27, 32]. However, the assumed similarity between soil extrusion patterns and those in metal extrusion processes remains unvalidated, while high extrusion pressures, localized consolidation, and air bubbles entrained during preparation of the soil sample introduce further uncertainties [25]. These factors complicate the correlation between p_e and c_u, particularly for soils with dissimilar plasticity and hydraulic conductivity properties [25]. Moreover, the extrusion mechanisms studied in RE tests share structural similarities with clay three-dimensional (3D) printing processes, indicating potential applications in optimizing clay formulation process.

X-ray computed tomography (CT) is a non-destructive imaging technique that can serve an important role in visualizing and quantifying soil behavior and soil–structure interactions within laboratory experiments [17, 30, 33]. For coarse-grained soils, X-ray CT has provided valuable insights into various mechanisms, such as strain localization [8], particle breakage [39], internal erosion [23], etc., thereby elucidating their impacts on the macroscopic behavior of these soils. Digital volume correlation (DVC), a technique comparing sequential X-ray scans, is effective in quantifying the 3D displacement fields [3], primarily for coarse-grained soils with discernible solid–void contrast and particle mineralogy [11, 29]. Operating at a resolution of several microns, X-ray CT facilitates particle-scale analysis, including tracking of individual sand particles, by utilizing their location and morphology information, thereby quantifying their kinematics [2, 11]. The particle-scale kinematical information provides more nuanced insights into shear band formation and reveals the influence of particle shape [1].

Characterizing deformation in fine-grained soils with X-ray CT poses challenges due to the sub-micron particle sizes, often being smaller than the imaging resolution. To overcome this, Birmpilis et al. [4] employed DVC, leveraging contrast between soil components (e.g., silt grains and clay matrix) in X-ray attenuation to measure 3D strain and displacement in fine-grained soils. DVC has also been applied to investigate the desiccation [10] and wetting behaviors of fine-grained soils [21]. Alternatively, the larger markers embedded in clay samples can be used to represent the deformation pattern of the surrounding soil matrix. For instance, platy mica particles embedded in kaolinite were tracked under one-dimensional compression [12] by comparing their shape parameters within a cylindrical searching region. Also, Xu et al. [37] adopted entrained air bubbles, as markers, to monitor internal deformation and desiccation crack formation in drying kaolinite pastes. Using an artificial neural network (ANN), air bubbles were linked between sequential X-ray CT scans, accounting for changes in the bubble geometry caused by drying-induced soil shrinkage. Recently, Wu et al. [36] proposed a two-step method, where particle tracking results from embedded sand particles were implemented to enhance DVC analysis. These studies demonstrate the potential of various techniques for analyzing the internal deformation of fine-grained soil samples.

This study investigates the internal deformation patterns during RE tests with X-ray CT. An X-ray-transparent extrusion apparatus was fabricated using strong plastic to characterize the internal deformation of three kaolinite samples, with embedded fine sand particles, prepared at various water contents. Sequential CT scans are performed during the RE process for each sample, enabling the tracking of individual sand grains to reveal detailed internal soil deformation and flow behaviors. Due to the complex internal deformation, we develop a guided marker-based tracking algorithm to optimize the size and shape of the searching zones, minimizing tracking errors, while considering the axisymmetric displacement field. Of the RE test the tracking results reveal distinct displacement patterns and provide new insights on the complex soil deformation and flow patterns of RE testing.

2 Experimental setup

Timár [31] performed a pioneering study on the extrusion of fine-grained soil, employing the direct-extrusion approach. A loading ram compressed a fine-grained soil sample contained in a metal chamber of bore cross-sectional area A_o. When sufficiently large, the applied force (F_e) caused soil extrusion to occur via an orifice, of area A_f, located centrally in the chamber base, with the extrusion ratio defined as $R = A_o / A_f$. However, the frictional resistance generated at the metal sidewall to soil interface, as the soil sample is pushed along the chamber length to extrude via the die opening, complicates the data interpretation. Thus, subsequent soil extrusion investigations by various researchers [15, 16, 20, 35] adopted the RE approach, in which the die orifice is centrally located in the loading ram, invariably using a soil chamber of 38-mm bore diameter and a 6-mm dia. orifice, giving an extrusion ratio of R = 40.1.

A comprehensive review of previous RE apparatus and experimental studies of fine-grained soils is presented in O'Kelly [25]. The applied force is continuously monitored during the course of the RE test, with the applied pressure value that causes extrusion to occur (i.e., $p_e = F_e / A_o$) proposed as a means of quantifying the c_u of fine-grained soils [14–16]. The primary advantage of the RE test over direct shear and triaxial tests is its simplicity in terms of the RE apparatus, testing procedure and test duration, requiring only a few minutes to complete each test [35]. Moreover, the RE test exhibits a similar ease of operation to the fall-cone test, while providing the distinct advantage of inducing a clear shear failure within clay samples, a feature not achievable by the fall-cone test.

However, an examination of RE tests performed on dissimilar fine-grained soils, employing the same extrusion ratio and ram displacement rate, revealed that the p_e / c_u ratio varies between soils [14, 25], leading to the present general unreliability of the RE tests (employing apparatus with $R \approx 40$) for c_u determination. Therefore, if further examined and standardized, the RE test could hold strong potential for wider adoption due to the simplicity and short duration for set up and completion of the RE test, requiring only a few minutes to complete [35]. By examining sequential X-ray CT scans and using an enhanced ANN tracking algorithm, this study focuses on characterizing the internal deformation mechanisms of the RE test by tracking fine sand particles that were embedded in the kaolinite samples undergoing extrusion.

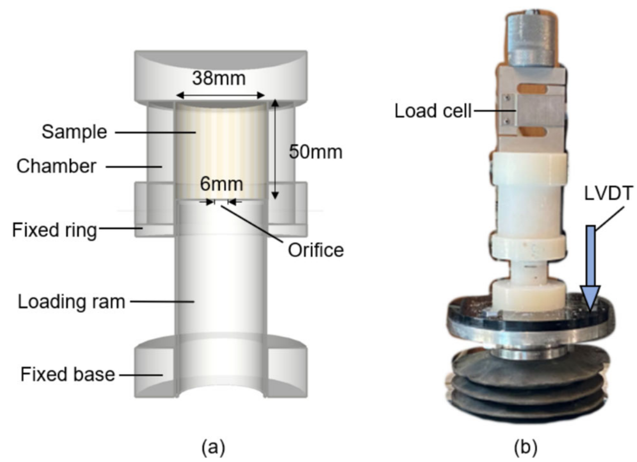

Fig. 1 Reverse extrusion testing: **a** schematic diagram of RE apparatus (not to scale); **b** photo of RE apparatus set up in a uniaxial loading machine

2.1 Reverse extrusion (RE) apparatus

For the present research, a nylon RE apparatus (Fig. 1a) was specially developed to facilitate X-ray CT scanning of the sample deformation patterns occurring at intervals during the RE tests. The inverted sample chamber of the RE apparatus had a bore diameter of 38 mm and was 50 mm deep. When set up in a uniaxial loading machine (Fig. 1b), the RE's detachable loading ram is moved vertically upwards, inside of the restrained sample chamber, to cause axial compression of the compacted soil therein. When the applied force is sufficiently large, downward extrusion of the soil occurs via a central 6-mm dia. orifice in the top of the hollow loading ram. The sample chamber and orifice diameters were set as 38 and 6 mm, respectively, resulting in an extrusion ratio of R = 40.1. These dimensions are commonly employed in previous RE investigations of fine-grained soils [25]. To prevent the fine sand markers that were embedded in the kaolinite samples from sticking and potentially interfering with the smooth relative movement of the RE's loading ram and chamber sidewall, the apparatus design provided a 1.0-mm-wide annular gap between them.

During the axial compression, the fixed base of the RE loading ram, which is positioned centrally on the platen of the uniaxial loading machine, is enlarged to avoid its tilting, as the ram is displaced upwards at a rate of 1 mm/min by a stepping motor. This displacement rate is typical of that employed in previous RE investigations and is deemed sufficiently fast for the undrained loading condition. A linear variable differential transformer (LVDT) transducer and a load cell recorded the ram displacement and the axial force acting across the length of the constrained sample. Periodically, the entire extrusion apparatus was carefully separated from the loading machine for performing a sequence of X-ray CT scans. During this process, using nylon screw fasteners, the fixed ring securely clamped the loading ram to the chamber, thereby preventing their relative movement, avoiding any disturbance to the soil sample.

2.2 Materials and sample preparation

The extrusion tests were performed on kaolinite pastes (IMERYS, Speswhite), with a measured fall-cone liquid limit (LL) of 67%, and a thread-rolling plastic limit of 37%. Fine quartz sand, with a particle-size range of 0.3–0.6 mm, a coefficient of curvature of 1.05, and a coefficient of uniformity of 1.37, was adopted as the internal markers. The density of quartz sand is $\sim$ 2.6 Mg/m^3, while the bulk density of the kaolinite samples varied between 1.40 and 1.75 Mg/m^3, depending on their water contents in the investigated range of w = 42–57%. As shown later, the large difference in the densities of the sand grains and the kaolinite particles produced a good contrast within the CT images. The fine sand was selected to balance imaging resolution with the number of data points. Specifically, the chosen particle-size range (of 0.3–0.6 mm) ensured sufficient voxels to resolve particle morphology, achieving a particle-to-voxel size ratio of $\sim$ 16. Furthermore, compared to larger particles, fine sand grains (at the same mass proportion relative to the fine-grained soil) offered a higher number of data points, enabling more effective characterization of the soil deformation pattern in the RE test.

The kaolinite–sand mixture was prepared using the following steps. First, de-aired water was thoroughly mixed with the kaolinite powder to create a paste with an initial water content of $\sim$ 100% (i.e., 1.5 $\times$ LL). Fine sand was then carefully mixed into the kaolinite paste, ensuring uniform distribution of the sand grains (markers) throughout the mixture. The sand particles constituted around 4.7% of the total volume of the kaolinite–sand mixture, resulting in an average spacing between adjacent sand grains of about twice their diameter ($\sim$ 35 voxels). Subsequently, subsamples of the mixture were allowed to air dry at ambient laboratory temperature for sufficient periods to achieve the targeted water contents. Note that the sand-to-kaolinite mass ratio varied among the tested kaolinite–sand samples with the same sand-to-kaolinite volume ratio, depending on the water content of kaolinite pastes. The samples were then allowed to homogenize overnight to ensure uniform moisture distribution. Finally, to prepare the homogenized mixture for extrusion testing, gentle pressure was applied using a palette knife to place the kaolinite–sand mixture into the RE chamber, ensuring it was almost completely full of the soil mixture without introducing excessive compaction.

2.3 Testing procedure and X-ray scanning

Extrusion testing was performed on kaolinite–sand samples prepared at three water contents of 57% (Sample 1; I_L = 0.67), 52% (Sample 2; I_L = 0.50) and 42% (Sample 3; I_L = 0.17), where I_L is the liquidity index. For each water content, an RE test was performed without scans. The red curves in Fig. 2 show the applied pressure against ram displacement traces for these tests. In the extrusion tests with X-ray CT scans (green curves), the sample was progressively loaded until the applied pressure reached the extrusion pressure (p_e), at which point the upward displacement of the RE loading ram was stopped. After a 10-min standing period, the pressure acting along the sample length had stabilized after stress relaxation. The fixed ring was then secured to clamp the RE loading ram to the sample chamber, and the entire extrusion apparatus was removed from the loading machine to perform the first scan (S1).

X-ray CT scans were conducted using a GE Phoenix Vtomex scanner, operated at a voltage of 120 kV, and a current of 310 μA. The RE apparatus was rotated on a precision rotating stage for 15 min. 4497 projections were collected to reconstruct X-ray images at a voxel size of 28 μm. Once scan S1 was completed, the RE apparatus was carefully reinstalled on the uniaxial loading machine. The loading platen was slowly displaced upwards to remove apparatus compliance and then stopped. The fixed ring was unfastened, allowing free movement between the RE loading ram and the sample chamber to occur with further displacement of the loading ram. The loading platen was displaced upwards again, causing an additional ram displacement of $\sim$ 2.5 mm. When the re-applied pressure matched the experimental curve for the sample tested earlier without CT scanning, the procedure was repeated to obtain the second scan (S2).

3 Image processing and analysis

3.1 Image processing

Figure 3a shows a typical horizontal slice for the scan S1 of Sample 1. The grayscale image presents distinct contrast between the markers (sand grains), kaolinite, entrained air bubbles, and the sidewall of the nylon extrusion chamber. Image processing was performed using Python in order to extract the markers from the grayscale images, and involved three main steps: (i) a median filter (kernel size: 3 $\times$ 3 $\times$ 3) was applied three times to balance noise

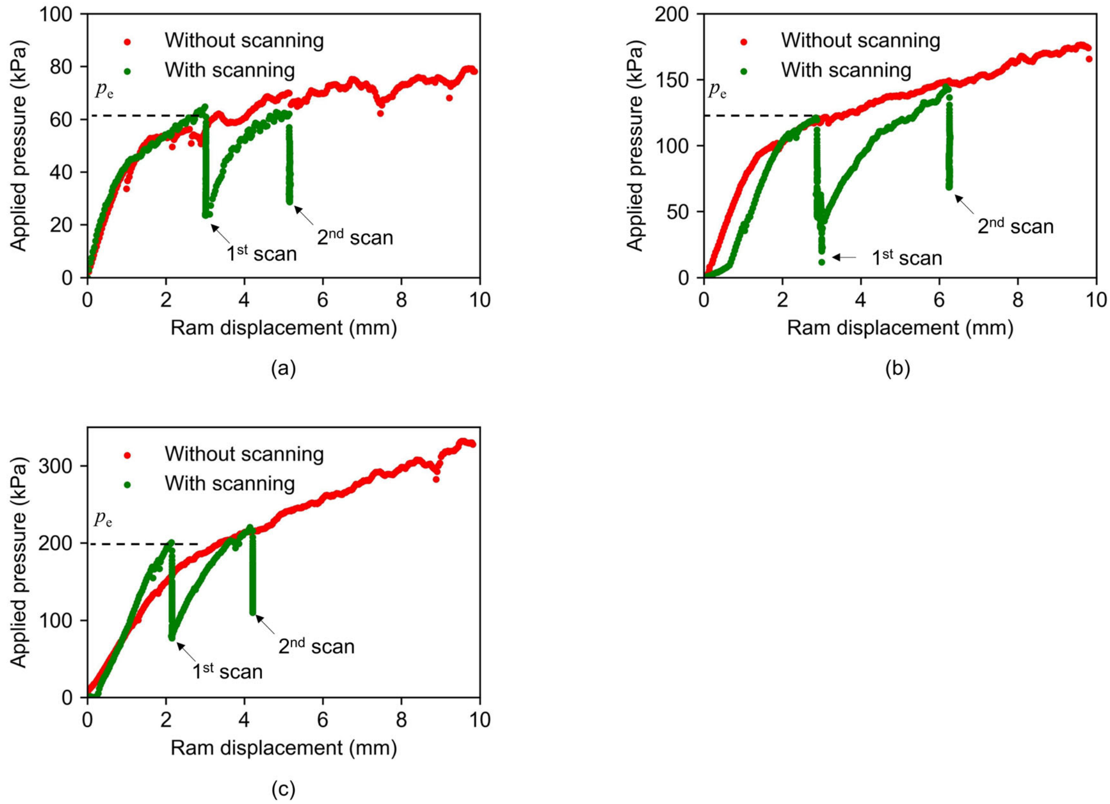

Fig. 2 Loading behaviors of kaolinite–sand samples at different water contents of **a** 57%, **b** 52%, and **c** 42%, with and without X-ray CT scans. Locations of the two scans (S1 and S2) are marked in the plots

reduction and detail preservation; (ii) a threshold value was determined manually, to separate the markers from the other phases, as shown in Fig. 3b; (iii) individual markers were labeled with unique identifications through a watershed segmentation, to distinguish between markers that were in close proximity (Fig. 3c). Note that, by comparing the volume consistency of manually linked markers associated with the scans S1 and S2, the threshold was verified, with differences of less than 2%. Figure 3d shows the 3D view of individual markers (sand grains) dispersed throughout the kaolinite–sand mixture for Sample 1, exhibiting a relatively uniform distribution. Each of the three tested kaolinite–sand sample pairs contained ~ 20,000 sand grains, with an average nearest-neighbor distance between grains of ~ 1.1 mm (standard deviation of ~ 0.17 mm).

3.2 Marker shape analysis

The location, size and shape parameters of individual markers (sand grains) were determined from the labeled images (details given in [37, 38]). The x, y and z locations of the markers were measured with respect to their centroids. Size parameters were calculated from the triangular surface mesh generated using the Marching Cube algorithm, including volume V, surface area SA, major dimension a, intermediate dimension b, and minor dimension c. Specifically, marker volume was obtained by dividing the volume into tetrahedrons and applying surface integrals. The shape of the markers was quantified using the sphericity $SP(=\sqrt[3]{36\pi V^2/SA})$ and aspect ratio AR $(=(b/a+c/b)/2)$ parameters. Figure 4 shows the distributions of typical marker size and shape parameters for the three kaolinite–sand samples. The mean volume of individual markers (sand grains) was 0.146 mm^3 (Fig. 4a), indicating a volume-equivalent diameter of 0.65 mm, with the major dimension varying primarily between a = 0.5 and 1.5 mm (average value of 0.89 mm) (Fig. 4b). Note that an inconsistence of volume distributions was observed between the three samples in Fig. 4a, which is likely attributed to the segmentation of markers at the different soil water contents. The SP and AR parameters for the individual markers were both found to vary mainly between 0.6 and 0.9 (Fig. 4c, d).

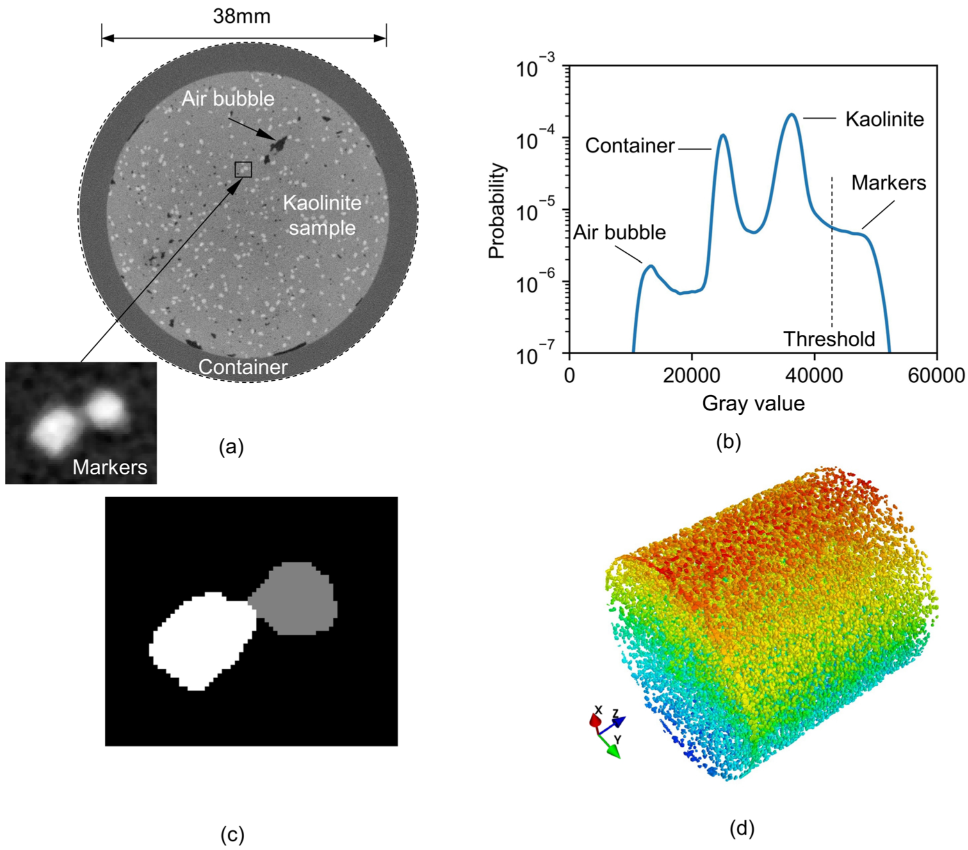

Fig. 3 Illustration of image processing: **a** typical grayscale horizontal slice; **b** histogram of gray value; **c** markers separated by watershed segmentation; **d** 3D visualization of individual markers, with the color indicating marker label

4 Marker tracking with artificial neural networks (ANN)

4.1 ANN-based tracking algorithm and training dataset

The ANN model links markers between two sequential scans based on the markers' size, shape, and location parameters. First, each marker in the scan S1 is compared with all markers in the scan S2 to define a correlation factor, in the range of 0 to 1, that indicates the possibility of correctly linking two markers between these scans. Then, a ranking algorithm establishes a unique linkage between the markers in the two scans according to the correlation factor. The marker-tracking procedure mainly includes three steps: (a) unification of the coordination systems across different scans; (b) training and validation of an ANN model based on manually linked markers; (c) implementation of the trained ANN model to all markers, and the creation of one-to-one linkages between the two scans. More details of the marker-tracking algorithm using ANN are described in Xu et al. [37].

For the kaolinite–sand Sample 1, we manually linked 300 pairs of markers between the scans S1 and S2. Using ImageJ software, the markers were paired based on their shape similarity and relative locations within marker clusters, ensuring accuracy. Figure 5 compares the size and shape parameters for the 300 manually linked marker pairs between the scans S1 and S2, with the markers ranked based on their parameter values in S1. Marker volume shows the highest consistence between the two scans, indicating higher accuracy in volume measurements (Fig. 5a). In contrast, the major dimension (a) and sphericity (SP) have a slightly larger scatter compared to marker volume (Fig. 5b, c). The aspect ratio (AR) parameter exhibits the largest scatter, of approximately $\pm$ 0.05, which is significant relative to the total AR variation of 0.4 (Fig. 5d). This scatter likely results from errors in determining the markers' orientations through principal component analysis. Thus, the marker volume parameter (V) emerges as the most reliable parameter for marker tracking due to its minimal relative error.

4.2 Tracking results and filtering algorithm

The performance of ANN models, each trained with one of nine distinct tracking parameter groupings, is summarized in Table 1. All models were trained using the 300 manually

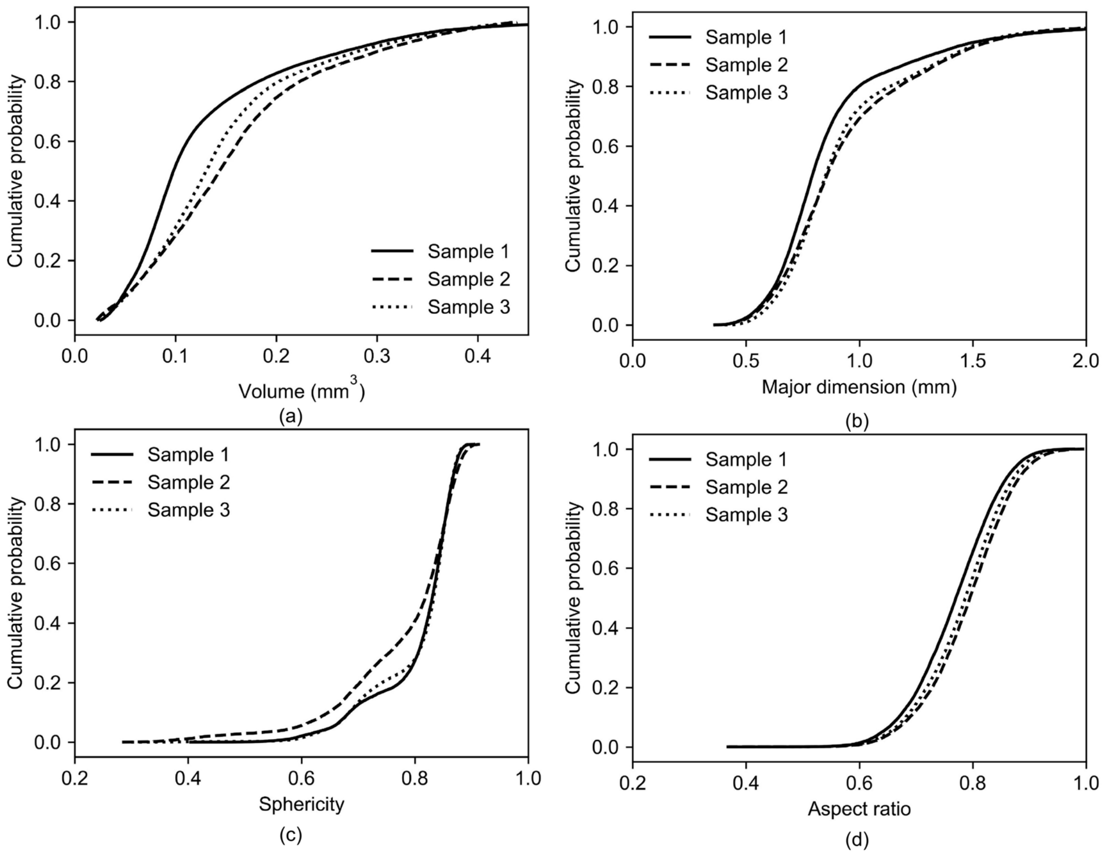

Fig. 4 Cumulative distributions of typical size and shape parameters for the sand particles (markers) embedded in the three kaolinite samples: **a** volume; **b** major dimension; **c** sphericity; **d** aspect ratio

linked marker pairs between the scans S1 and S2 for Sample 1. These models were subsequently tested to evaluate their tracking accuracy, and to calculate correlation factors for all of the markers in Sample 1. ANN models based on the parameter groupings 1, 2 and 3 produced very low tracking accuracy ($\leq$ 16.5%), emphasizing the critical role of incorporating the marker location information (Δx, Δy and Δz) into the tracking algorithm. This finding highlights that marker size and shape parameters alone are insufficient to reliably differentiate between individual markers, particularly given the large number of markers (sand grains) in the kaolinite–sand sample and their narrow particle-size range (of 0.3 to 0.6 mm). In contrast, the parameter groupings 4 to 9, which included marker location information along with size and/or shape parameters, significantly improved the tracking accuracy to over 82%, as listed in Table 1. Grouping 9, which integrates the marker location (Δx, Δy, Δz), size (ΔV, ΔSA, Δa, Δb, Δc) and shape (ΔAR) parameters, produced the highest tracking accuracy of 91.78%. Furthermore, when applied to all of the markers in Sample 1, the ANN model trained on grouping 9 produced the highest mean correlation factor of 0.83.

Figure 6a shows the displacement field on a vertical plane (x–z) with a 5-mm out-of-plane thickness, obtained using the ANN model trained with the grouping 9 parameter combination. Along the vertical axis, z = 0 represents the top (closed end) of the sample chamber, and the 6-mm dia. orifice is centered at (x, z) = (19 mm, 37.5 mm). The results in Fig. 6a reveal two distinct regions, divided approximately at $z \approx$ 20 mm, with markedly different deformation patterns evident. As expected, the soil located near the orifice exhibits significantly larger deformations compared to the upper sample region. Although the overall deformation pattern is captured effectively, inconsistencies in the direction and magnitude of the displacement vectors are evident near the orifice, when compared to neighboring vectors. The tracking accuracy of the nine parameter groupings was also compared across the two regions of Sample 1: i.e., the lower region near the orifice (at the loading ram), and the upper region near the closed end of the sample chamber. Results showed a considerably lower tracking accuracy for the lower region, where the sample deformations are influenced by the 'flow' and extrusion of soil through the orifice, compared to the more stable upper region. To address this issue, a filtering algorithm was

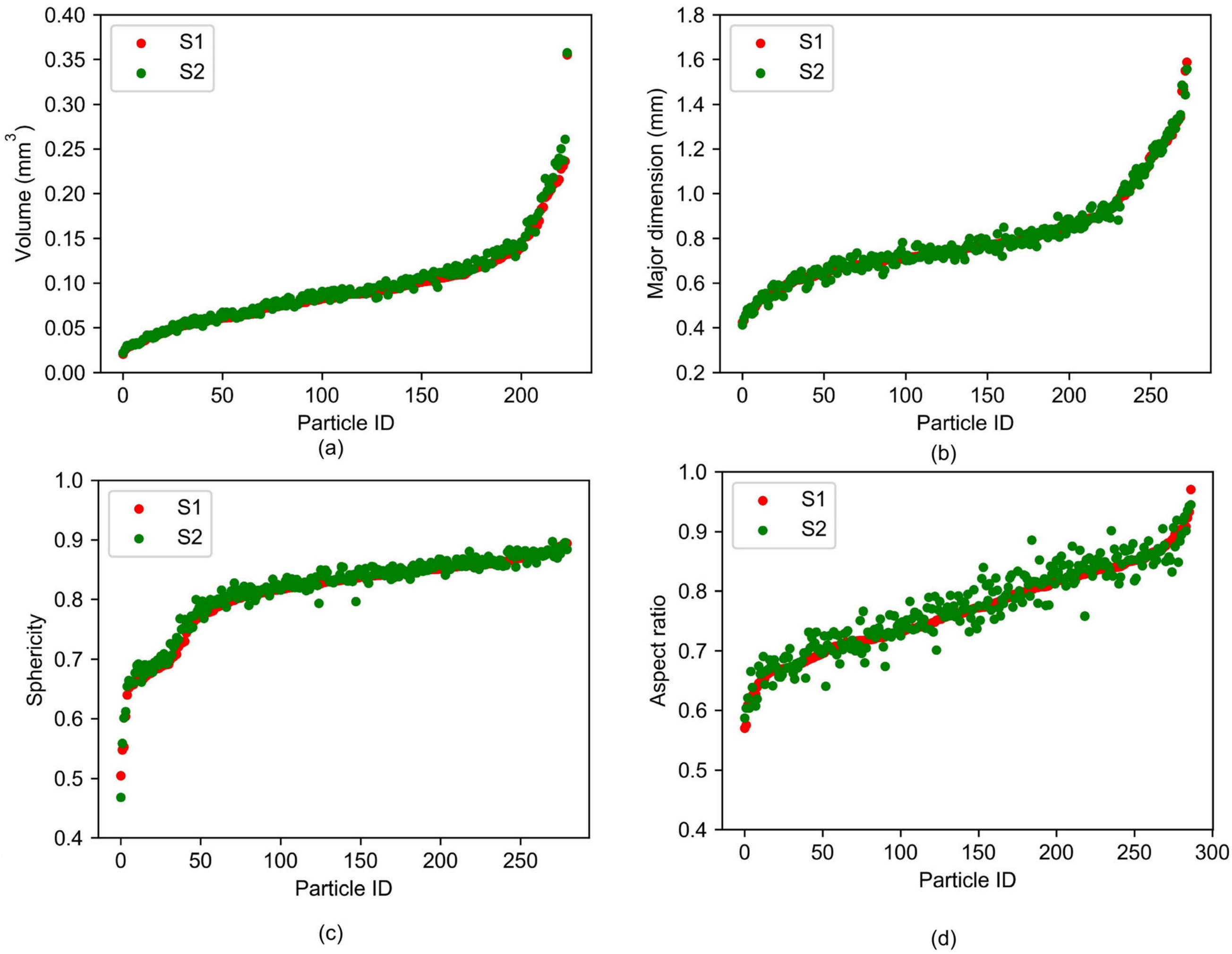

Fig. 5 Comparison of size and shape parameters for the manually linked markers between scan S1 and S2 for the kaolinite–sand Sample 1: **a** volume; **b** major dimension; **c** sphericity; and **d** aspect ratio parameters

applied to remove anomalous displacement vectors. The filtering criterion involved calculating the average displacement within a 1.5-mm radius for each marker, and discarding vectors whose magnitudes exceeded three times this local average. As evident from Fig. 6b, this approach effectively eliminates significant outliers while preserving the integrity of the overall displacement pattern. Note that any markers located adjacent to the orifice in the scan S1 were extruded from the sample chamber, while the markers located near the orifice in the scan S2 experienced substantial displacements.

4.3 Influence of searching zones

As indicated in Table 1, the tracking accuracy of the ANN models is mainly influenced by the marker location information. Consequently, the varied deformation patterns across different regions of the sample can adversely affect the tracking accuracy. Specifically, the ANN model may generalize its learning from the upper region of the sample, where small displacements occur, and apply it to the lower region in which significantly larger displacements occur (or vice versa). Moreover, the displacement trends within the lower region exhibit substantial variation. Hence, it can be concluded that marker location changes (i.e., Δx, Δy, Δz) should be excluded from the ANN model to mitigate the impact of diverse displacement patterns on the tracking accuracy. However, ANN models that relied only on marker geometry parameters across the entire sample achieved very low tracking accuracy, indicated by the poor performance of the parameter groupings 1, 2 and 3, as listed in Table 1. To address this limitation, i.e., to restrict the number of markers considered for comparison, a cubic searching zone (centered on each marker's location in the scan S1) was introduced. Among the tested parameter groupings (of 1, 2 and 3) that did not rely on marker location information, the grouping 2 was found to produce the highest tracking accuracy and was applied. Figure 7a

Table 1 Performance of different parameter combinations in terms of (i) tracking accuracy for manually linked markers, and (ii) correlation factors for all markers

Grouping number	Parameters	Tracking accuracy (%)			Correlation factor		
		Total	Upper sample region	Lower sample region	Mean	Standard deviation	RMSE
1	ΔV, ΔSP, Δa	1.36	1.34	1.39	0.17	0.04	0.69
2	ΔV, ΔSA, ΔAR, Δa, Δb, Δc	16.50	16.04	17.00	0.46	0.11	0.32
3	ΔV, ΔSA, ΔSP, ΔAR, Δa, Δb, Δc	15.82	14.70	17.00	0.42	0.12	0.38
4	Δx, Δy, Δz, ΔV, ΔSA	82.87	96.64	68.53	0.77	0.33	0.16
5	Δx, Δy, Δz, ΔV, ΔSP	82.19	96.64	67.13	0.78	0.31	0.14
6	Δx, Δy, Δz, ΔSP, ΔAR	87.33	97.32	76.92	0.77	0.35	0.41
7	Δx, Δy, Δz, ΔV, ΔSA, Δa, Δb, Δc	91.44	97.32	85.31	0.81	0.32	0.13
8	Δx, Δy, Δz, ΔV, ΔSA, ΔSP, ΔAR, Δa, Δb, Δc	91.44	96.64	86.01	0.80	0.34	0.16
9	Δx, Δy, Δz, ΔV, ΔSA, ΔAR, Δa, Δb, Δc	91.78	97.31	86.01	0.83	0.29	0.11

shows the evolution of tracking accuracy as the side length (L) of the searching box reduces from $\propto$ to 80 voxels. The results show a significant increase in tracking accuracy as L reduces to 100 voxels, followed by a decline as L further decreases from 100 to 80 voxels. Thus, the optimal tracking accuracy for the parameter grouping 2 of 67% occurred for a search box size of $L = 100$ voxels, which closely corresponds to the maximum marker displacement observed between the scans S1 and S2 of the Sample 1.

Due to the significant variation in displacement magnitude across different regions in the sample, the size of the searching zones was further optimized based on the marker's location (x, y, z) using a deep learning model (Model-D). Model-D predicts the potential displacement vectors for each marker location, which were then used to refine the size of the search box for each marker. The model was designed following established deep learning principles [6], using the '*adam*' optimizer, with mean squared error as the loss metric, and trained over 5000 epochs. Model-D was trained on the locations and displacement vectors of the 300 manually linked marker pairs from scans S1 and S2 for Sample 1, enabling it to predict the potential displacement vector magnitude (u_x, v_y, w_z) for any marker location. To prevent underestimating of the searching box size centered on the marker location in scan S1, its side lengths were set to three times the predicted displacement magnitude (i.e., $3u_x$, $3v_y$, $3w_z$). The predicted searching zones (L_p) from Model-D produced an overall tracking accuracy of $\sim$ 80%, as presented by the orange data point in Fig. 7a. However, despite this improvement, the displacement field still exhibited some noise and anomalies, particularly in the lower sample region, i.e., near the orifice end, where large deformations occurred (Fig. 7b).

4.4 Guided marker tracking

To further enhance the tracking accuracy achieved for the parameter grouping 2, the axisymmetric nature of the internal soil flow toward the orifice was considered, with the geometry of the searching zones confined to triangular prisms, each centered at the identified marker location in scan S1 (Fig. 8). This use of irregular geometry for the searching zones, combined with the displacement magnitude predicted by Model-D, constitutes a 'guided' tracking approach. The horizontal projection of the triangular prism searching zone forms an isosceles triangle oriented toward the sample's longitudinal axis (Fig. 8a). The dimensions of the searching zone were determined as $Lp_z = 3w_z$ and $Lp_{xy} = 3\sqrt{u_x^2 + v_y^2}$, as shown in Fig. 8b, with their sizes estimated using Model-D. Implementing this flow-trend-based searching zone for the parameter grouping 2 improved the accuracy of the marker tracking to 90.6% and increased the averaged correlation factor to 0.82, which is at a similar level to those achieved for the parameter grouping 9 incorporating particle location information. Figure 9a presents the resulting smooth displacement field predicted for Sample 1, demonstrating significantly reduced noise compared to that evident in Figs. 6b and 7b. Notably, the number of successfully tracked markers reached 21,013; a considerable increase compared to Fig. 6b (19,804) and Fig. 7b (20,875).

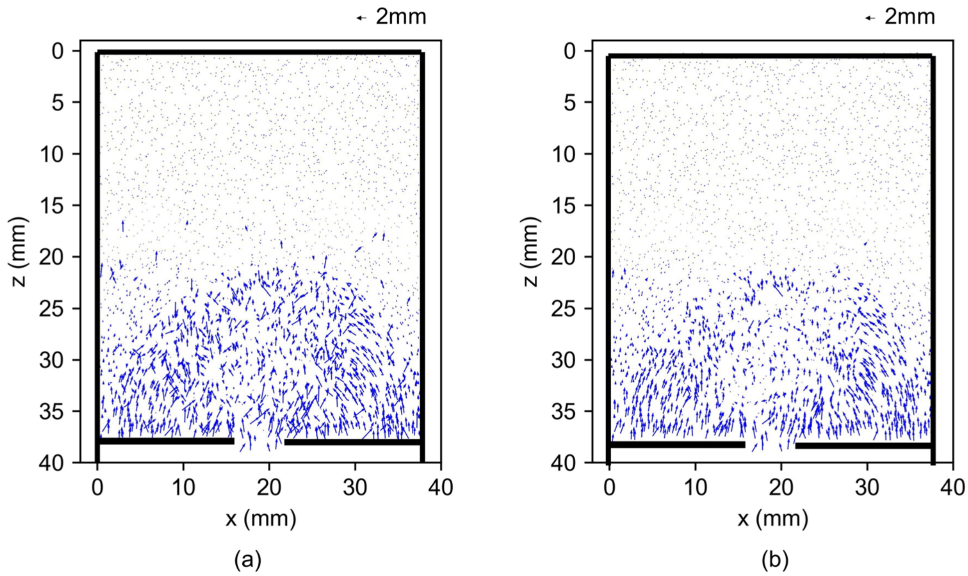

Fig. 6 Projection of displacement fields on *x*–*z* plane at the middle of Sample 1, deduced using ANN model trained by the grouping 9 parameters: **a** original displacement field; **b** displacement field after filtering

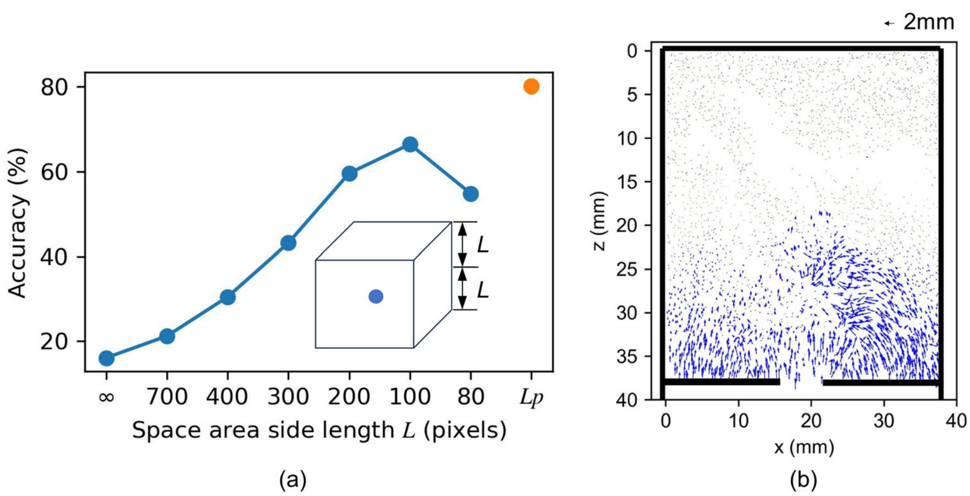

Fig. 7 **a** Variation of the tracking accuracy with size of the cubic searching zone for the parameter grouping 2 (refer to Table 1). **b** Displacement field for Sample 1 generated using searching zone sized by deep learning model (after filtering). *Note* L_p (i.e., orange data point) is the searching zone predicted by Model-D

5 Soil deformation patterns in RE tests

5.1 Overall displacement field

A vertical section of Sample 1, centered on the sample axis and with an out-of-plane thickness of 5 mm (i.e. y = 16.5–21.5 mm), was selected for analysis. The projection of the displacement vectors onto the x–z plane is presented in Fig. 9a. The displacement field distinctly separates into two regions (i.e., located above and below z = 20 mm), with markedly different displacement patterns evident. In Region 1 (i.e., near the orifice end), the soil experienced an arch-shaped displacement trend. As the loading ram moved upwards, penetrating further into the sample container, the soil exhibited arch-shaped deformation, resulting in the downward extrusion of a 6-mm diameter soil thread via the central orifice. During this process, the mean vertical displacement (of 2.12 mm) for the markers located near the loading ram was found to closely match the ram displacement (of 2.10 mm), as recorded by the LVDT measurements. In contrast, much smaller marker displacements occurred in the Region 2, i.e., located near the closed end of the sample chamber. Figure 9b provides the 3D view of the displacement vectors, revealing a dome-shaped region near the orifice, with the dome's exterior delineating the shear failure surface.

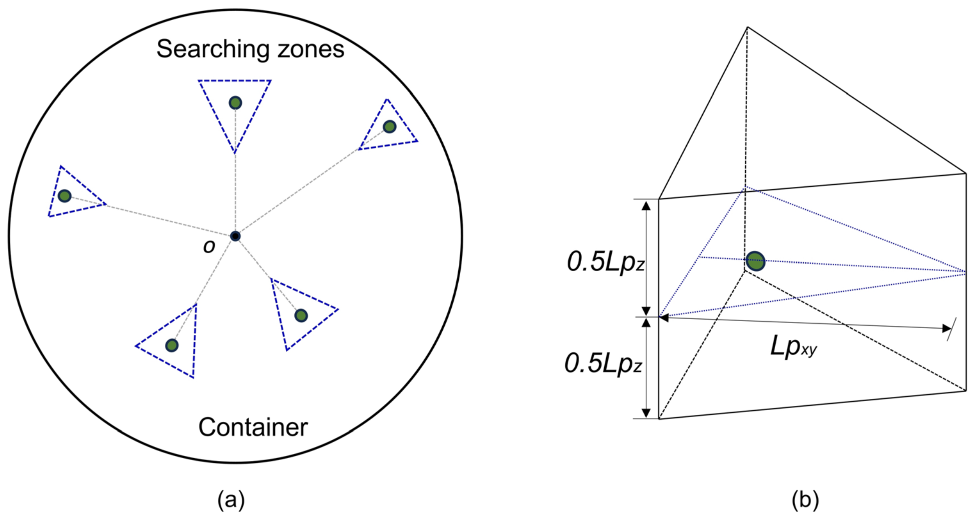

Fig. 8 Illustration of searching zones for guided marker tracking: **a** horizontal view of several searching zones; **b** 3D view of searching zone

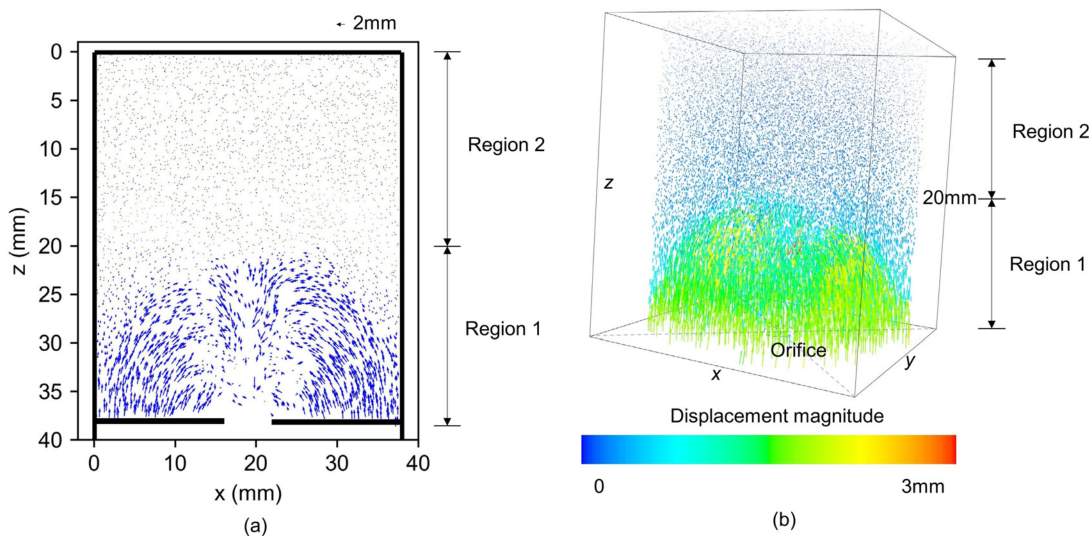

Fig. 9 Displacement field of Sample 1 after filtering: **a** projection of displacement vectors on the x–z plane; **b** 3D view of displacement field

The results confirm that the initial sample length (of ∼ 40 mm) was more than sufficient to prevent any interaction between the dome failure surface and the closed-end boundary condition of the sample chamber.

5.2 Region 1: Shearing and extrusion

Figure 10 shows a close-up view of the displacement field in Region 1, which is further subdivided into four areas, labeled A to D. In Areas A, the displacement vectors indicate that soil wedges were pushed upward by the advancing loading ram, undergoing relatively large vertical displacements. The chamber sidewall (interface) has a considerable localized impact on the displacement pattern of these wedges, although its impact diminished substantially at a short inward radial distance. In Areas B, the soil

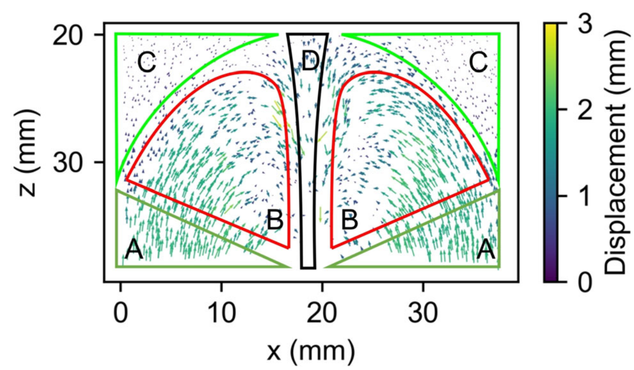

Fig. 10 Projection of displacement field on the x–z plane within y = 16.5 to 21.5 mm for Region 1 of Sample 1 (note the deformation pattern is separated into four distinct areas labeled Areas A–D)

was pushed by the underlying wedges of Areas A. This behavior resembles the radial-shear zone described in bearing capacity theory for shallow circular foundations. However, instead of the foundation penetrating the soil, the reverse happens here, with the soil being extruded via the orifice. The displacement direction in Areas B transitions from upwards and radially inwards near the chamber sidewall to radially downward as it approaches the central orifice. Areas C lie above Areas B and exhibit much smaller displacement vectors, with a curved shear surface separating these regions. In contrast, Area D shows downward movement with large displacements, as the soil in this region is directed toward and extruded through the central orifice. Considering the apparatus extrusion ratio of $R = 40.1$, the downward displacement of the soil occurring near the orifice is approximately 40 times greater than the upward displacement of the loading ram. This means that the 2.1 mm of ram displacement recorded between the scans S1 and S2 of Sample 1 corresponds to a downward displacement of $\sim$ 80 mm for the extruded soil thread. Tracking such large displacements in Area D poses significant challenges, and even manual linking of markers in this area between scans is often not feasible. Furthermore, the markers located near to and directly above the orifice are particularly difficult to track, leading to a reduced number of tracked markers in this region. Consequently, the small displacement vectors observed within Area D of Fig. 10 do not fully represent the actual extrusion speed, which is considerably higher in this central region.

All displacement vectors in Region 1 of Sample 1 were categorized into different areas (i.e., Areas A–D), with the resulting distributions of displacement for Areas A to C shown in Fig. 11. Statistical analysis for Area D was not feasible due to insufficient data, as explained above. Axial displacement (d_a) is movement along the depth of the sample. Radial displacement (d_r) is measured from the sample's central axis (positive when moving outward, negative when moving inward). Circumferential displacement (d_c) refers to tangential movement (positive for counterclockwise, negative for clockwise). Referring to Fig. 11a, Area A is predominantly characterized by a large upward vertical displacement (d_a), approaching the actual loading ram displacement value of 2.1 mm occurring between the scans S1 and S2. In contrast, both the radial and circumferential displacements are much smaller. The circumferential displacement follows a normal distribution, centered at zero, whereas the radial displacement is normally distributed around – 0.3 mm, indicating a slight inward trend. In Area B, the radial displacement markedly increases toward the sample center, with the average data centered at approximately -1 mm (see Fig. 11b), whereas Area C has considerably diminished displacements, mostly less than $\pm$ 0.5 mm (Fig. 11c).

5.3 Region 2: compression

Adjacent to the closed end of the sample chamber (i.e., far from the loading ram and orifice), the soil in Region 2 is anticipated to experience limited deformation. This is confirmed in Fig. 12a, which presents the projection of the displacement field onto the x–z plane, revealing a non-uniform displacement pattern, with the primary displacements being vertical, and a maximum displacement value of only $\sim$ 0.3 mm. The compressibility of the soil in Region 2 is predominantly attributed to the compression of entrained air bubbles, which respond to the extrusion force applied across the length of the sample. Figure 12b shows the contour plot of vertical displacement for the Region 2, revealing that the deformations in this region are influenced by the soil stresses transmitted from the underlying Region 1. For instance, at the bottom boundary of Region 2, the vertical displacements are smaller at the center, where the soil located directly above the orifice (i.e. in Area D of Region 1) is moving downward at a significant rate to extrude via the orifice. Furthermore, in Region 2, the vertical displacement occurring near the sidewall is reduced due to boundary interference. Thus, the non-uniform deformation pattern in Region 2 arises from a combination of uneven soil stresses transmitted from the underlying Region 1, as well as sidewall boundary interference, and the distribution of entrained air bubbles.

5.4 Deformation characteristics across the three investigated samples with different water contents

The displacement patterns in Region 1 for the three investigated samples were obtained from comparing the scans S1 and S2 for each sample (see Fig. 13). As the water content decreases within the investigated range of w = 42–57%, overall, the deformation patterns remain largely unchanged, indicating that the impact of water content variation on the deformation pattern is minimal within this range (i.e., for I_L = 0.17 to 0.67). All three samples exhibited a consistent arch-like deformation pattern in Region 1, with similar contributions experienced from the sidewall boundary. Furthermore, Fig. 14 shows the variation of the mean vertical displacement with depth in Region 2 for all three samples. As shown, the vertical displacement increases linearly with depth (measured down from the closed end of the sample chamber), starting from zero at $z = 0$, and increasing linearly to $\sim$ 0.15 mm of upward displacement at z = 15 mm. This linearity results in an averaged vertical strain ($\overline{\epsilon_z}$) in Region 2 of $\sim$ 0.01 (i.e., calculated as 0.15/15). This small compression is likely due to the reduction in the volume of

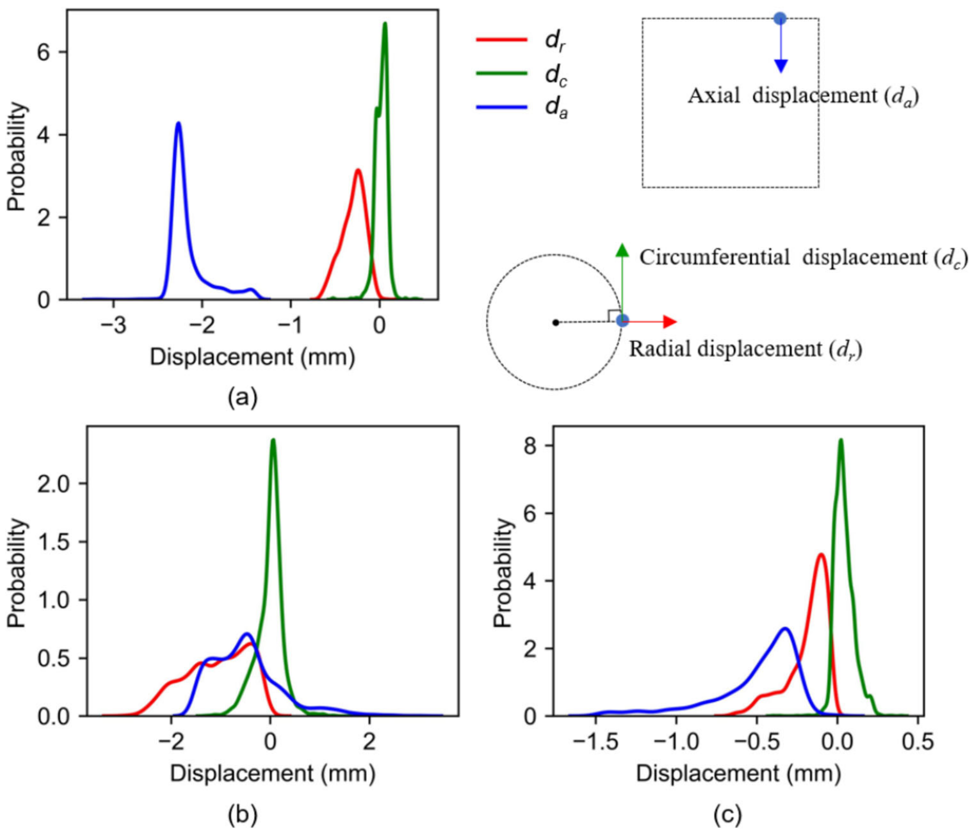

Fig. 11 Distribution of displacement in different areas of Region 1 for Sample 1: **a** Area A; **b** Area B; **c** Area C

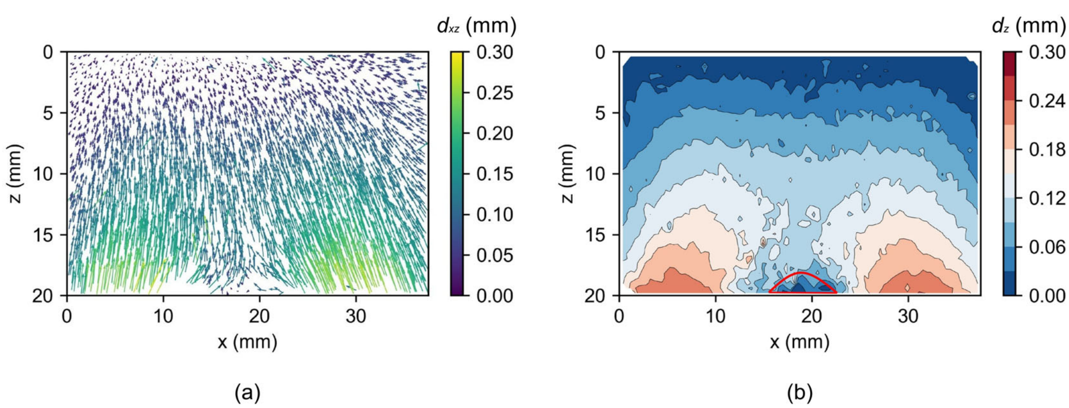

Fig. 12 Deformation patterns in Region 2 of Sample 1 within y = 15 to 25 mm: **a** projection of displacement vectors on x–z plane; **b** vertical displacement contour plot

entrained air bubbles, whose presence within the samples was confirmed by the X-ray CT scans (e.g. see Fig. 3a). The averaged vertical strain is marginally different between the three samples, as shown in Fig. 14, which may be attributed to minor variations in their initial volumes of entrained air bubbles.

Using image processing techniques, the volume of air bubbles present in Region 2 of Sample 1 was examined to investigate its relative impact on the results. For the scan S1, which had a total volume of 19,273 mm^3 for Region 2, the air bubble volume was estimated to be $\sim$ 346.7 mm^3, representing an air void content of 1.8%. In scan S2, the air bubble volume had decreased to $\sim$ 221.5 mm^3, equating to an air void content of 1.2%. Consequently, the volumetric strain (and hence the averaged vertical strain for 1D compression conditions) due to this reduction in air bubble volume for Region 2 was computed to be $\overline{\epsilon_z} \approx 0.65\%$, which approximately matches the $\sim$ 1.0% value deduced from the data plots in Fig. 14. Therefore, the compression in Region 2 is confirmed as primarily due to the

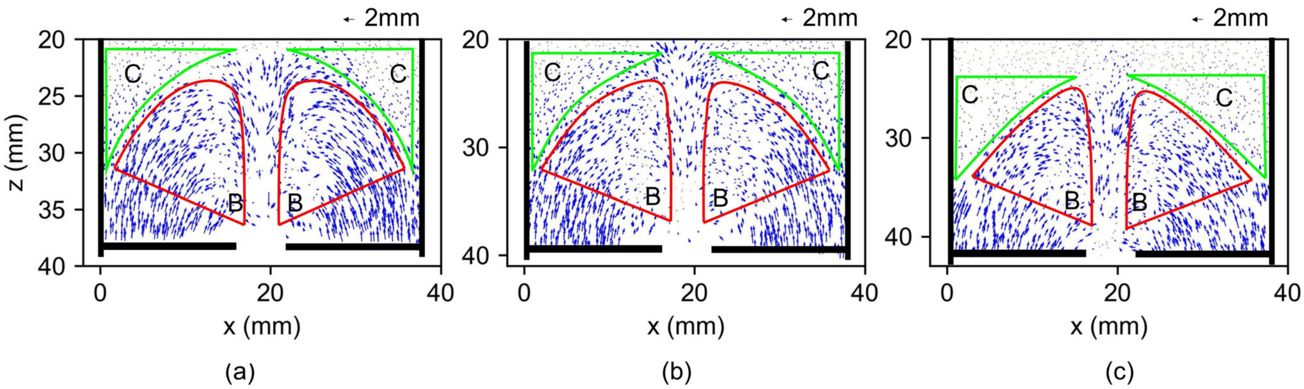

Fig. 13 Projection on x–z plane of displacement field in Region 1 for **a** Sample 1 (w = 57%), **b** Sample 2 (w = 52%) and **c** Sample 3 (w = 42%)

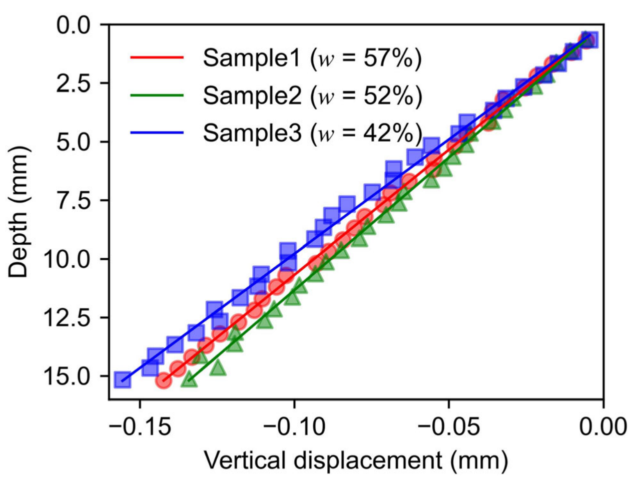

Fig. 14 Variation of mean vertical displacement along depth in Region 2 for the three kaolinite–sand samples

compression of entrained air bubbles. In contrast, the impact of consolidation is expected to be minimal, given the loading ram displacement rate of 1 mm/min resulted in short-duration extrusion testing stages, the fine-grained nature of the soil (i.e., its low permeability), and the significantly reduced pressures acting on the samples during the ~ 30-min intervening period between scans S1 and S2.

5.5 RE flow pattern

The flow pattern observed for RE testing of the slightly sandy kaolinite soil examined in the present study differs dramatically from the previous conceptual model proposed for RE testing of fine-grained soils [15, 16, 35]. These researchers had assumed that the model shown in Fig. 15a, originally developed for direct-extrusion testing of metals, could also be applied to the RE testing of fine-grained soils. In this model, the material in the 'Shear zone' of the cylindrical test billet is expected to distort, shear, and extrude via the orifice upon the application of the extrusion pressure, while the material above the 'Shear zone' (i.e., within the Rigid zone) and in the 'Dead zone' is assumed to remain undeformed. This conceptual model is typically used in metal extrusion processes, where materials exhibit plastic flow and continuum behavior [9, 28]. In the present study, the RE behavior observed in the testing of fine-grained soil reveals a distinctly different flow mechanism, as shown in Fig. 15b. Specifically, soil wedges form directly above the upwardly advancing loading ram and mobilize the overlying soil in Region 1, creating a stress 'rotation' zone. Here, the shear surface within Region 1 consists of two distinct parts: one part aligns along the interface between the chamber sidewall and the soil wedges (interface shear), while the second part is composed of arched shear surfaces occurring within the soil sample, as indicated by the red surfaces in Fig. 15b. Along these arched failure surfaces, the shear stress equals the undrained shear strength (c_u) of the soil, which may vary from the shear capacity (c^*_u) mobilized at the sidewall interface. Above the shear surface, the soil undergoes a slight compression, with smaller upward displacements occurring near the sample's axis and next to the chamber sidewall. As the loading ram moves steadily upward causing the soil to extrude downward via the orifice, the arched shear surfaces gradually propagate upward through the soil sample, thereby maintaining a stable flow pattern throughout.

6 Conclusion

This study investigated the internal flow pattern of kaolinite samples undergoing RE testing using X-ray tomography and a marker-base tracking method enhanced by artificial neural networks (ANN). An innovative X-ray transparent RE apparatus was developed to facilitate scans without causing disturbance of the soil samples contained in the extrusion chamber. Fine sand particles served as

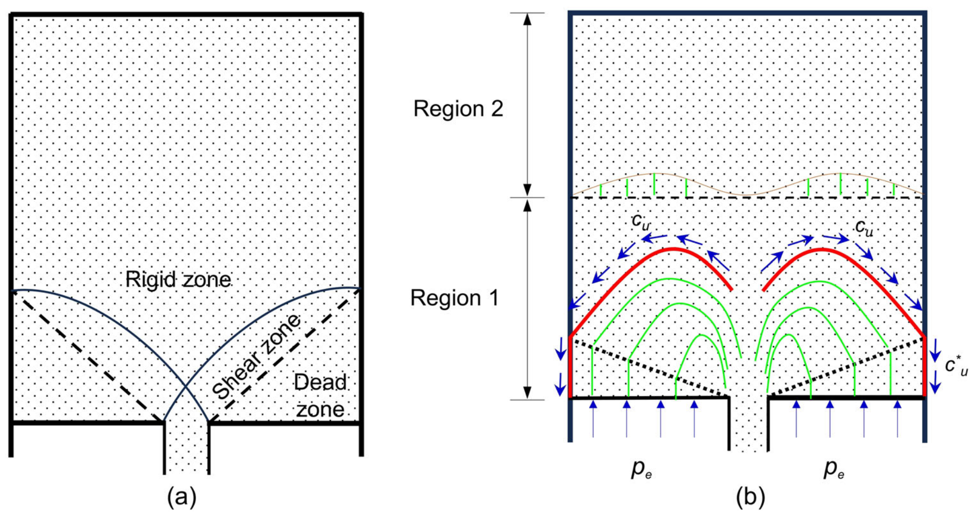

Fig. 15 Flow mechanisms in the RE test: **a** previous model for metals (following Whyte [35]); **b** updated model for fine-grained soil testing, based on measured displacement fields in the present study

embedded markers within the kaolinite samples. Image processing techniques, including filtering, threshold-based segmentation, and watershed labeling, enabled the determination of the marker characteristics, such as their location (x, y, z), size (volume, surface area, dimensions), and shape parameters (sphericity and aspect ratio). Validation with manually linked markers demonstrated excellent consistency across scans, with marker volume exhibiting the highest accuracy and reliability for marker-tracking purposes.

ANN models were employed to link markers across sequential scans, with a combination of marker location, size and aspect ratio parameters producing the highest tracking accuracy. However, complex displacement fields occurring throughout the sample undergoing RE testing challenged the use of particle location as a tracking parameter. To overcome this, a guided marker-tracking algorithm was developed, featuring flow-trend-based searching zones shaped as isosceles triangular prism geometries aligned with axisymmetric displacement fields. Additionally, the size of the searching zone was adjusted considering the displacement magnitude of the training dataset. This tracking method, which excluded particle location as a parameter, achieved a tracking accuracy of 90.6% and an average correlation factor of 0.82.

This study of the internal flow pattern of fine-grained soil undergoing RE testing identified two distinct deformation regions in all three samples investigated with different water contents. The soil in Region 1 (i.e., nearest the orifice end, and extending approximately half the loading ram diameter in depth) exhibited significant deformation that was characterized by an arch-shaped shear failure surface combined with pronounced downward extrusion occurring via the central orifice. Within this region, four sub-areas showed distinct deformation patterns: triangular soil wedges were pushed upwards (Areas A), leading to shear-induced dome formation (Areas B) and minimal displacement zones (Areas C). Directly above the orifice (Area D), the large downward soil displacements posed tracking challenges. Despite variations in water content between the three investigated samples, the deformation patterns in Region 1 were found to remain broadly consistent, indicating limited influence of water content variation within the investigated range (of $I_L = 0.17$ to 0.67).

Whereas Region 2, nearest the closed end of the sample chamber, experienced minimal soil deformation, with a vertical strain averaging only 0.01. This strain was attributed to the reduction in the air bubble volume within the soil sample (i.e., rather than consolidation, as the short duration of the RE tests limited consolidation effects) resulting from the extrusion force that acted across the sample length. The small soil displacements occurring in Region 2 resulted from the non-uniform stress transmission from the underlying Region 1, the effect of sidewall friction, and the compression of entrained air bubbles.

The observed overall flow pattern significantly deviates from previously assumed RE models applied for fine-grained soils, revealing arched shear surfaces, and stress rotation zones, as well as the influence of chamber sidewall friction and entrained air bubbles. These findings underscore the need to refine existing assumptions in RE analysis, as applied to testing of fine-grained soils, to account for these complex deformation mechanisms. This research provides a foundation for developing improved RE models that accurately capture these intricate behaviors.

Acknowledgements S. Xu acknowledges the financial support of the China Scholarship Council (CSC award no. 202106567007) as a Visiting PhD Student at University College Dublin (UCD). Access to the X-ray CT scanning facilities at the UCD Rosemount Environmental Research Station is grateful acknowledged.

Funding Open Access funding provided by the IReL Consortium.

Data availability The data that support the findings of this study are available from the corresponding author upon request.

Declarations

Conflict of interest The authors have no competing interests to declare relevant to this article's content.

References

1. Alshibli KA, Jarrar MF, Druckrey AM, Al-Raoush RI (2017) Influence of particle morphology on 3D kinematic behavior and strain localization of sheared sand. J Geotech Geoenviron Eng 143:04016097. https://doi.org/10.1061/(ASCE)GT.1943-5606.0001601
2. Andò E, Hall SA, Viggiani G, Desrues J, Bésuelle P (2012) Grain-scale experimental investigation of localised deformation in sand: a discrete particle tracking approach. Acta Geotech 7:1–13. https://doi.org/10.1007/s11440-011-0151-6
3. Bay BK, Smith TS, Fyhrie DP, Saad M (1999) Digital volume correlation: three-dimensional strain mapping using X-ray tomography. Exp Mech 39:217–226. https://doi.org/10.1007/BF02323555
4. Birmpilis G, Andò E, Stamati O, Hall SA, Gerolymatou E, Dijkstra J (2022) Experimental quantification of 3D deformations in sensitive clay during stress-probing. Géotechnique. 73:655–666. https://doi.org/10.1680/jgeot.21.00114
5. Bozozuk M (1972) Downdrag measurements on a 160-ft floating pipe test pile in marine clay. Can Geotech J 9:127–136. https://doi.org/10.1139/t72-014
6. Chollet F (2018) Deep learning with Python. Manning Publications Co, Shelter Island, New York
7. Das BM (2017) Shallow foundations: bearing capacity and settlement, Third edition. CRC Press, Boca Raton, FL, USA.
8. Desrues J, Chambon R, Mokni M, Mazerolle F (1996) Void ratio evolution inside shear bands in triaxial sand specimens studied by computed tomography. Géotechnique 46:529–546. https://doi.org/10.1680/geot.1996.46.3.529
9. Dieter GE (1976) Mechanical metallurgy. New York: McGraw-hill.
10. El Hajjar A, Ouahbi T, Eid J, Hattab M, Taibi S (2020) Shrinkage cracking of unsaturated fine soils: new experimental device and measurement techniques. Strain 56:e12352. https://doi.org/10.1111/str.12352
11. Hall SA, Bornert M, Desrues J, Pannier Y, Lenoir N, Viggiani G, Bésuelle P (2010) Discrete and continuum analysis of localised deformation in sand using X-ray μCT and volumetric digital image correlation. Géotechnique 60:315–322. https://doi.org/10.1680/geot.2010.60.5.315
12. Ibeh CU, Pedrotti M, Tarantino A, Lunn RJ (2021) PLATY-MATCH—a particle-matching algorithm for the analysis of platy particle kinematics using X-ray computed tomography. Comput Geotech 138:104367. https://doi.org/10.1016/j.compgeo.2021.104367
13. Kayabali K (2011) Assessment of shear strength at consistency limits—a reappraisal. Electronic J Geotech Eng 16:1679–1695
14. Kayabali K, Ozdemir A (2013) Use of reverse extrusion method to determine undrained shear strength. Geotech Geol Eng 31:719–727. https://doi.org/10.1007/s10706-013-9621-y
15. Kayabali K, Tufenkci OO (2010) Determination of plastic and liquid limits using the reverse extrusion technique. Geotech Test J 33:102209. https://doi.org/10.1520/GTJ102209
16. Kayabali K, Tufenkci OO (2010) Shear strength of remolded soils at consistency limits. Can Geotech J 47:259–266. https://doi.org/10.1139/T09-095
17. Khaddour G, Riedel I, Andò E, Charrier P, Bésuelle P, Desrues J, Viggiani G, Salager S (2018) Grain-scale characterization of water retention behaviour of sand using X-ray CT. Acta Geotech 13:497–512. https://doi.org/10.1007/s11440-018-0628-7
18. Kvalstad TJ, Nadim F, Kaynia AM, Mokkelbost KH, Bryn P (2005) Soil conditions and slope stability in the Ormen Lange area. Mar Petrol Geol 22:299–310. https://doi.org/10.1016/j.marpetgeo.2004.10.021
19. Lizárraga JJ, Buscarnera G (2018) Safety factors to detect flow-slides and slips in unsaturated shallow slopes. Géotechnique 68:442–450. https://doi.org/10.1680/jgeot.17.T.003
20. Medhat F, Whyte IL (1986) An appraisal of soil index tests. EGSP 2:317–323. https://doi.org/10.1144/GSL.1986.002.01.55
21. Molinero Guerra A, Aimedieu P, Bornert M, Cui Y-J, Tang AM, Sun Z, Mokni N, Delage P, Bernier F (2018) Analysis of the structural changes of a pellet/powder bentonite mixture upon wetting by X-ray computed microtomography. Appl Clay Sci 165:164–169. https://doi.org/10.1016/j.clay.2018.07.043
22. Muraro S, Jommi C (2021) Experimental determination of the shear strength of peat from standard undrained triaxial tests: correcting for the effects of end restraint. Géotechnique 71:76–87. https://doi.org/10.1680/jgeot.18.P.346
23. Nguyen CD, Benahmed N, Andò E, Sibille L, Philippe P (2019) Experimental investigation of microstructural changes in soils eroded by suffusion using X-ray tomography. Acta Geotech 14:749–765. https://doi.org/10.1007/s11440-019-00787-w
24. O'Kelly BC (2013) Atterberg limits and remolded shear strength–water content relationships. Geotech Test J 36:939–947. https://doi.org/10.1520/GTJ20130012
25. O'Kelly BC (2019) Reappraisal of soil extrusion for geomechanical characterisation. Geotech Res 6:265–287. https://doi.org/10.1680/jgere.19.00006
26. O'Kelly BC, Vardanega PJ, Haigh SK (2018) Use of fall cones to determine Atterberg limits: a review. Géotechnique 68:843–856. https://doi.org/10.1680/jgeot.17.R.039
27. Pua LM, Caicedo B, Castillo D, Caro S (2018) Development of a 3D clay printer for the preparation of heterogeneous models. In: McNamara A, Divall S, Goodey R, Taylor N, Stallebrass S, Panchal J (eds) physical modelling in geotechnics, 1st edn. CRC Press, pp 155–160
28. Saha PK (2000) Aluminum extrusion technology. ASM International, USA, p 259
29. Takano D, Lenoir N, Otani J, Hall SA (2015) Localised deformation in a wide-grained sand under triaxial compression revealed by X-ray tomography and digital image correlation.

Soils Found 55:906–915. https://doi.org/10.1016/j.sandf.2015.06.020
30. Thakur MM, Penumadu D (2020) Triaxial compression in sands using FDEM and micro-X-ray computed tomography. Comput Geotech 124:103638. https://doi.org/10.1016/j.compgeo.2020.103638
31. Timar A (1974) Testing the plastic properties of cohesive and intermediate-type soils by extrusion. Acta Tech Acad Scientiarum Hungaricae 76:355–370. https://doi.org/10.1016/0148-9062(82)91670-9
32. Verástegui-Flores RD, Di Emidio G (2014) Assessment of clay consistency through conventional methods and indirect extrusion tests. Appl Clay Sci 101:632–636. https://doi.org/10.1016/j.clay.2014.09.033
33. Wang J-P, Luan J-Y, Gao X-G, Liu T-H, Andò E, François B (2022) A micro-investigation of unsaturated sand in mini-triaxial compression based on micro-CT image analysis. Acta Geotech 17:4799–4821. https://doi.org/10.1007/s11440-022-01658-7
34. Westerberg B, Müller R, Larsson S (2015) Evaluation of undrained shear strength of Swedish fine-grained sulphide soils. Eng Geol 188:77–87. https://doi.org/10.1016/j.enggeo.2015.01.007
35. Whyte IL (1982) Soil plasticity and strength—a new approach using extrusion. Ground Eng 15:16–24
36. Wu M, Wang J, Pan B, Yin Z-Y (2024) Particle tracking-aided digital volume correlation for clay–sand soil mixtures. Géotechnique 75:760–772. https://doi.org/10.1680/jgeot.24.00036
37. Xu S, Lai J, O'Kelly BC, Zhao B (2023) 3D deformation and strain fields in drying kaolinite obtained from tracking internal bubbles using X-ray CT and ANN. Acta Geotech 19:99–113. https://doi.org/10.1007/s11440-023-01948-8
38. Zhao B, Wang J (2016) 3D quantitative shape analysis on form, roundness, and compactness with μCT. Powder Technol 291:262–275. https://doi.org/10.1016/j.powtec.2015.12.029
39. Zhao B, Wang J, Andò DE, Viggiani DG, Coop M (2020) An investigation of particle breakage under one-dimensional compression of sand using X-ray micro-tomography. Can Geotech J 57:754–762. https://doi.org/10.1139/cgj-2018-0548